Tetragonal polymorph of $BaFe_2S_2O$ as an antiferromagnetic Mott insulator

Shi-Jie Song,[1] Yi-Qiang Lin,[1] Bai-Zhuo Li,[1] Si-Qi Wu,[1] Qin-Qing Zhu,[2] Zhi Ren,[2] and Guang-Han Cao[1,3,*]

[1]*Department of Physics, Zhejiang University, Hangzhou 310027, China*

[2]*School of Science, Westlake Institute for Advanced Study, Westlake University, Hangzhou 310064, China*

[3]*Zhejiang Province Key Laboratory of Quantum Technology and Devices, Interdisciplinary Center for Quantum Information, and State Key Lab of Silicon Materials, Zhejiang University, Hangzhou 310027, China*

(Received 10 February 2022; revised 10 April 2022; accepted 3 May 2022; published 13 May 2022)

We report a tetragonal polymorph of $BaFe_2S_2O$ synthesized under high pressures. This β-$BaFe_2S_2O$ phase is structurally characterized by two-dimensional Fe_2O square nets that are sandwiched by sulfur atomic layers. The electrical, magnetic, and thermodynamic measurements indicate that it is an antiferromagnetic insulator with a Néel temperature of 121 K. A successive magnetic transition at ~40 K is observed, possibly associated with spin canting due to Dzyaloshinskii-Moriya interactions. Density functional theory based calculations reveal Mott localization driven by the on-site electron-electron Coulomb repulsion. The calculations also suggest a noncollinear Fe^{2+}-spin structure with two-$\mathbf{k}$ [$\mathbf{k_1} = (1/2, 0, 1/2)$ and $\mathbf{k_2} = (0, 1/2, 1/2)$] propagation vectors, primarily due to the magnetocrystalline anisotropy as well as the next-nearest-neighbor superexchange interactions mediated by oxygen and sulfur anions, respectively.

DOI: 10.1103/PhysRevMaterials.6.055002

I. INTRODUCTION

Electron correlations play an important role for the emergence of high-T_c superconductivity in copper oxides [1,2] and in iron pnictides/chalcogenides [3,4]. Cuprate superconductors can be viewed as a doped Mott insulator with the on-site Coulomb repulsion, the Hubbard U_H, much bigger than the bandwidth W [2]. In comparison, the electron correlation strength of iron-based superconductors is moderate, with $U_H \sim W$ [4,5]. Interestingly, the oxygen-incorporated variants of iron chalcogenides, $La_2Fe_2Ch_2O_3$ (Ch = S, Se), show enhanced electron correlations through band narrowing [6] and orbital-selective Mott localization [7,8]. Thus, in the sense of electron-correlation effects, such iron oxychalcogenides may bridge the gap between the two classes of high-T_c superconductors.

$La_2Fe_2Ch_2O_3$, first reported in the early 1990's [9], contain block layers of $[Fe_2OCh_2]^{2-}$ and fluorite-type $[La_2O_2]^{2+}$, stacking alternatingly along the crystallographic c axis. With the replacement of $[La_2O_2]^{2+}$ layers, analogous compounds of $Sr_2F_2Fe_2Ch_2O$ and $Ba_2F_2Fe_2Ch_2O$ were synthesized and investigated [10]. The characteristic $[Fe_2OCh_2]^{2-}$ block layers bear obvious differences with the common anti-fluorite-type layers of $[Fe_2As_2]^{2-}$ in iron-pnictide superconductors. In the middle of the Fe_2OCh_2 layers, there is the anti-CuO_2-like Fe_2O plane, in which Fe atoms are linearly coordinated with two oxygen anions. Fe atoms are also surrounded by four Ch^{2-} anions, resulting in a mixed-anion coordination octahedron of FeO_2Ch_4. These FeO_2Ch_4 octahedra share their faces, forming the $[Fe_2OCh_2]^{2-}$ infinite layers (see the inset of Fig. 1).

Additional oxychalcogenides with the Fe_2OCh_2 layers have been reported [11–16], since the discovery of iron-based superconductors [3]. All these materials show insulating behaviors with an antiferromagnetic (AFM) transition at $T_N \sim$ 100 K. The AFM structure is rather unusual, consisting of orthogonally intersecting one-dimensional AFM chains, which can be described with two propagation vectors, $\mathbf{k_1} = (1/2, 0, 1/2)$ and $\mathbf{k_2} = (0, 1/2, 1/2)$ [15–22]. This particular double-q spin structure is revealed to be dominated by two orthogonal next-nearest-neighbor interactions [17,18] where the magnetocrystalline anisotropy due to spin-orbit coupling plays an important role for the noncollinear spin structure [15,18].

Among those iron oxychalcogenides, the tetragonal polymorph of β-$BaFe_2Se_2O$, which could be synthesized only under high pressures [15], stands out because of nonstaggered stacking of the Fe_2OCh_2 layers (see the inset of Fig. 1). Like other iron oxychalcogenides, it is also an AFM insulator with $T_N = 106$ K. As a comparison, the ambient-pressure-synthesized orthorhombic polymorph (α-$BaFe_2Se_2O$) has a spin-ladder structure, showing AFM ordering at 240 K [23–25]. Its sibling spin-ladder iron sulfide, α-$BaFe_2S_2O$, shows AFM spin ordering at 260 K [26]. As we know, anion substitutions/replacements may tune physical properties with "applying chemical pressures" in the field of iron-based superconductors [27–29], therefore, it is appealing to explore the tetragonal polymorph of β-$BaFe_2S_2O$.

In this paper, we report our successful synthesis of β-$BaFe_2S_2O$ using a high-pressure strategy. The crystal structure was determined by a Rietveld refinement. The electrical, magnetic, and thermodynamic properties were measured, which indicate that it is an AFM insulator with $T_N = 121$ K. We also observed a successive magnetic transition at ~40 K, which gives rise to weak ferromagnetism. Our first-principles

*Corresponding author: ghcao@zju.edu.cn

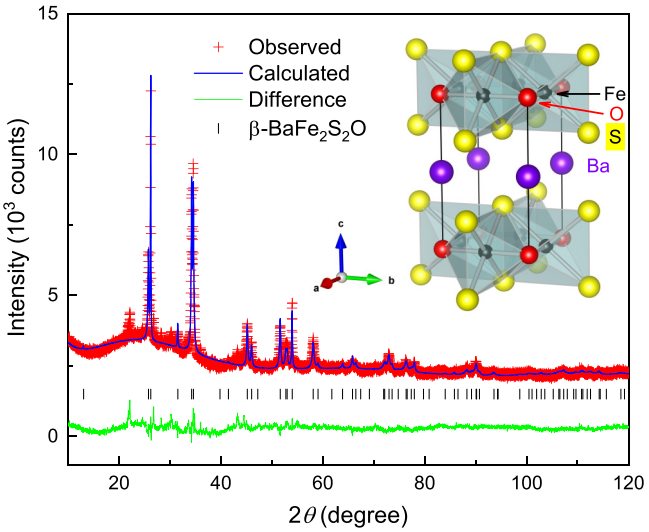

FIG. 1. Powder x-ray diffraction at room temperature and its Rietveld refinement profile of β-$BaFe_2S_2O$. The crystal structure of β-$BaFe_2S_2O$ is shown in the inset.

calculations suggest that the title material is a Mott insulator with the common noncollinear two-**k** spin structure.

II. EXPERIMENTAL METHODS

The polycrystalline sample of β-$BaFe_2S_2O$ was synthesized under high pressures and high temperatures using a piston-cylinder press (QUICKpress, Depths of the Earth). The source materials of BaO (99.5% Alfa Aesar), S (99.9995% Alfa Aesar), and Fe (99.99% Alfa Aesar), in the stoichiometric ratio, were mixed and milled in an argon-filled glovebox. The ground mixtures prereacted at 800 °C for 24 h in an alumina tube jacketed with a silica ampule. After that, the precursor was reground and pressed into a pellet. The pellet, wrapped with Pt foils, was then subjected to a pressure of 3.5 GPa in the QUICKpress apparatus. The high-pressure synthesis was carried out at 950 °C for 2 h. The final product obtained was black and dense, and was stable under ambient conditions.

The as-prepared sample was characterized by powder x-ray diffractions (XRD) using a PANalytical diffractometer (Empyrean Series 2) with Cu-$K_{\alpha 1}$ radiation. The crystal structure was refined by Rietveld analysis using the RIETAN-FP software [30]. Measurements of electrical resistivity and heat capacity were performed on a Quantum Design Physical Property Measurement System (PPMS-9). In the resistivity measurement, a standard four-electrode method was employed. The sample was cut into a thin rectangular bar, on which electrodes were made using silver paste and gold wires. The dc magnetization was measured on a Quantum Design Magnetic Property Measurement System (MPMS3).

We also performed the first-principles calculations based on density functional theory (DFT) using VASP package [31]. The exchange-correlation energy was treated using generalized-gradient-approximation (GGA) functionals [32] with or without rotationally invariant on-site Coulomb interaction corrections ($+U$) [33]. The plane-wave energy cutoff for all calculations was set to 600 eV. Spin-orbit interaction was included in the self-consistent calculations.

TABLE I. Room-temperature crystallographic data of β-$BaFe_2S_2O$, obtained from the Rietveld refinement of powder x-ray diffraction ($R_{wp} = 3.47\%$ and $S = 1.79$). The occupancy of each atom was fixed to 1.0 in the Rietveld refinement.

Chemical formula			$BaFe_2S_2O$		
Space group			$P4/mmm$ (No. 123)		
a (Å)			4.004(2)		
c (Å)			6.778(4)		
ρ (g/cm^3)			5.029		
Atom	site	x	y	z	U_{iso} (Å^2)
Ba	1b	0	0	1/2	0.0051
Fe	2f	0	1/2	0	0.010
S	2h	1/2	1/2	0.2472(10)	0.013
O	1a	0	0	0	0.015

III. RESULTS AND DISCUSSION

A. Crystal structure

Figure 1 shows the XRD pattern of the β-$BaFe_2S_2O$ sample synthesized at high pressures. Except for some minor unknown peaks, the main reflections can be well indexed using a tetragonal unit cell with $a \approx 4.01$ Å and $c \approx 6.78$ Å, suggesting formation of the target phase. The crystal structure was refined by Rietveld analysis using the internal structural parameters of the isostructural compound $Rb_{0.83}V_2Te_2O$ [34] as the initial input. The resultant structural parameters are presented in Table I.

The a and c parameters refined are 1.7% and 5.2% smaller, respectively, than those of the sibling compound β-$BaFe_2Se_2O$ [15]. This is directly due to the replacement of Se by S, which in general induces a chemical pressure. The relatively small reduction of the a axis dictates a strong rigidity of in the ab plane with Fe_2O sheets. On the other hand, the significant reduction of the c axis pushes the system toward three dimensionality. It is also noted that the theoretical density of this β-$BaFe_2S_2O$ phase is 15.5% higher than that of α-$BaFe_2S_2O$ (4.355 g/cm^3) [26], consistent with high-pressure stabilization of the β phase. In addition, the bond valence sum (BVS) [35] of the Fe ions is calculated to be 2.13, which is close to the formal Fe valence of +2.

The structural properties of β-$BaFe_2S_2O$ are compared with those of other related iron oxychalcogenides in Table II. Expectedly, in all the compounds, the lattice constants of an oxysulfide are systematically smaller than those of its corresponding oxyselenide. Note that the β-$BaFe_2S_2O$ phase holds the lowest a axis. Consequently, the interatomic distances of Fe-O, Fe-Fe, and Fe-S are all smallest among the oxychalcogenides. Nevertheless, the height of S atoms from the Fe_2O plane, h_{Ch}, of β-$BaFe_2S_2O$ is not the lowest and, similarly, the bond angle of S-Fe-S, α, is not the largest. This is because the oxychalcogenides with $[Ba_2F_2]^{2+}$ layers have exceptionally large a axis, which reduces h_{Ch} and increases α.

TABLE II. Comparison of structural and physical properties of the iron oxychalcogenides with Fe_2OCh_2 layers (Ch = S and Se). h_{Ch} stands for the height of Ch atoms from the Fe_2O plane, and α is the bond angle of Ch-Fe-Ch along a or b direction. T_N is the Néel temperature and E_a denotes the activation energy derived from the resistivity measurement.

Compound	a (Å)	c (Å)	$d_{Fe\text{-}O}$ (Å)	$d_{Fe\text{-}Ch}$ (Å)	$d_{Fe\text{-}Fe}$ (Å)	h_{Ch} (Å)	α (°)	T_N (K)	E_a (eV)	Refs.
$La_2O_3Fe_2Se_2$	4.0849(6)	18.5865	2.044(1)	2.724(1)	2.891(1)	3.603(1)	97.24	90.1	0.19 [6]	[22]
$La_2O_3Fe_2S_2$	4.0397	17.8782	2.021(1)	2.663(1)	2.858(1)	3.469(1)	98.76	107.2	0.24 [6]	[22]
$Sr_2F_2Fe_2Se_2O$	4.0925(2)	18.580(1)	2.046(1)	2.727(1)	2.894(1)	3.605(3)	97.24	95-97	–	[10]
$Sr_2F_2Fe_2S_2O$	4.0400(6)	17.998(4)	2.020(1)	2.633(1)	2.857(1)	3.377(1)	100.22	106.2	0.10, 0.28 [17]	[10]
$Ba_2F_2Fe_2Se_2O$	4.1946(6)	19.522(4)	2.097(1)	2.734(1)	2.966(1)	3.507(4)	100.21	83.6	0.28	[10]
$Ba_2F_2Fe_2S_2O$	4.1238(2)	19.089(1)	2.062(1)	2.649(2)	2.916(1)	3.325(5)	102.24	94–95	–	[10]
$Na_2Fe_2Se_2O$	4.107(8)	14.641(8)	2.053(5)	2.777(4)	2.904(6)	3.739(3)	95.37	73	0.26	[12]
$Na_2Fe_2S_2O$	4.0325(1)	14.077(1)	2.015(1)	2.670(2)	2.850(1)	3.503(1)	98.02	–	–	[36]
$BaFe_2Se_2O$	4.0748(1)	7.1501(5)	–	–	–	–	–	106	0.14	[15]
$BaFe_2S_2O$	4.004(2)	6.778(4)	2.002(2)	2.610(5)	2.831(3)	3.348(3)	100.2	121	0.15	This work

B. Physical properties

Figure 2 shows the resistivity measurement data for the as-prepared polycrystalline sample of β-$BaFe_2S_2O$. The room-temperature resistivity is about 100 Ω cm, comparable to that of the sibling compound β-$BaFe_2Se_2O$ [15]. The resistivity increases with decreasing temperature, basically obeying the Arrhenius equation, $\rho(T) = \rho_0 \exp[E_a/(k_B T)]$, where ρ_0 is the pre-exponential factor, E_a is the activation energy and k_B is Boltzmann constant. The result demonstrates that the title material is virtually an insulator. Fitting the $\rho(T)$ data from 150 to 300 K with the Arrhenius equation, one obtains an activation energy of $E_a = 0.15$ eV, which is very close to that of β-$BaFe_2Se_2O$ (0.14 eV) [15]. Note that the activation energy gives a lower limit of the energy band gap, $E_g \geqslant 2E_a = 0.30$ eV.

Figure 3 displays the temperature dependence of magnetic susceptibility $\chi(T)$ for β-$BaFe_2S_2O$. The high-temperature $\chi(T)$ data follow the extended Curie-Weiss law, $\chi(T) = \chi_0 + C/(T + \theta_W)$. This is in contrast to the broad hump of $\chi(T)$ due to two-dimensional short-range magnetic correlations in $La_2Fe_2Se_2O_3$ [6,22], $A_2F_2Fe_2Ch_2O$ (A = Ba, Sr) [10], and $Na_2Fe_2Se_2O$ [12]. Thus the Curie-Weiss paramagnetic behavior suggests dominantly three-dimensional magnetism, in accordance with the enhanced three dimensionality in β-$BaFe_2S_2O$. The Curie-Weiss fit from 200 to 400 K yields $\chi_0 = 0.00265$ emu mol^{-1} fu^{-1} (fu stands for formula unit), $C = 3.26$ emu K mol^{-1} fu^{-1} (or 1.63 emu K mol^{-1} Fe^{-1}), and $\theta_W = 360$ K. The large value of temperature-independent χ_0 could be due to the partial short-range magnetic correlations and/or possible Van-Vleck paramagnetism. With the fitted C value, the effective magnetic moment of Fe ions is derived to be $\mu_{eff} = 3.6\,\mu_B$/Fe, which is significantly smaller than that of high-spin Fe^{2+} ($4.9\,\mu_B$). The reduced effective magnetic moment can be explained in terms of (i) the partial short-range magnetic correlations and (ii) the d-p hybridizations. The positive value of θ_W indicates dominant AFM interactions between Fe^{2+} spins. Note that the fitted θ_W value is much higher than the AFM transition temperature, $T_N = 121$ K (see below). This implies that there are still short-range AFM

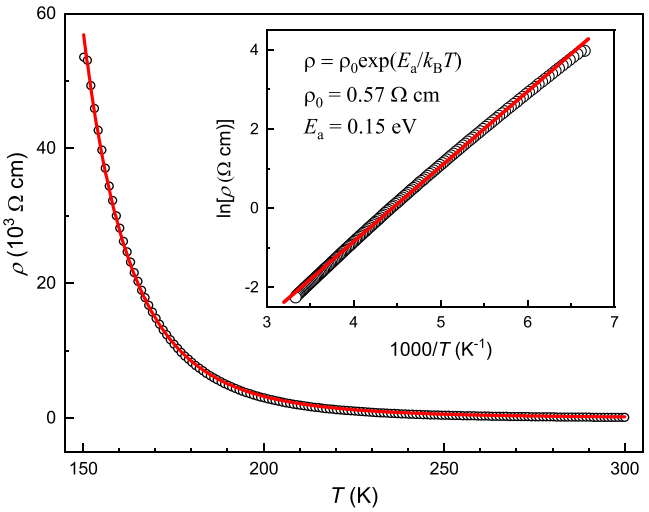

FIG. 2. Temperature dependence of resistivity for the β-$BaFe_2S_2O$ polycrystalline sample. The inset shows the plot of $\ln\rho$ vs $1/T$. The red line is the fit with the Arrhenius equation.

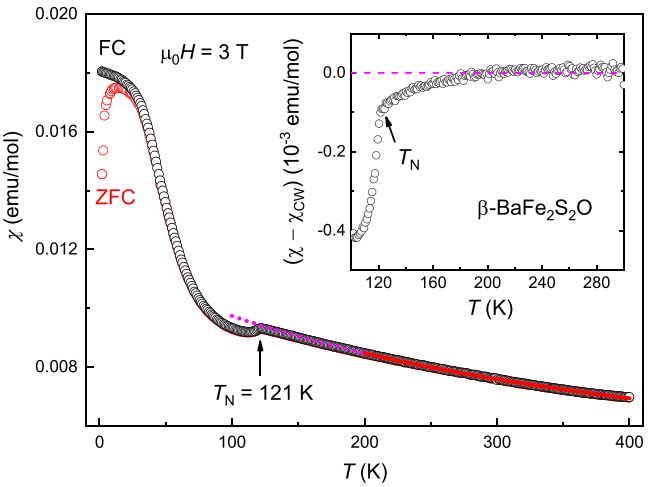

FIG. 3. Temperature dependence of magnetic susceptibility of β-$BaFe_2S_2O$ measured at a 3-T field in field-cooling (FC) and zero-field-cooling (ZFC) protocols. The red solid line is the Curie-Weiss (CW) fit, and the pink dashed line is the extrapolation. Deviations from the extrapolated CW formula are plotted in the inset. The antiferromagnetic Néel temperature is marked.

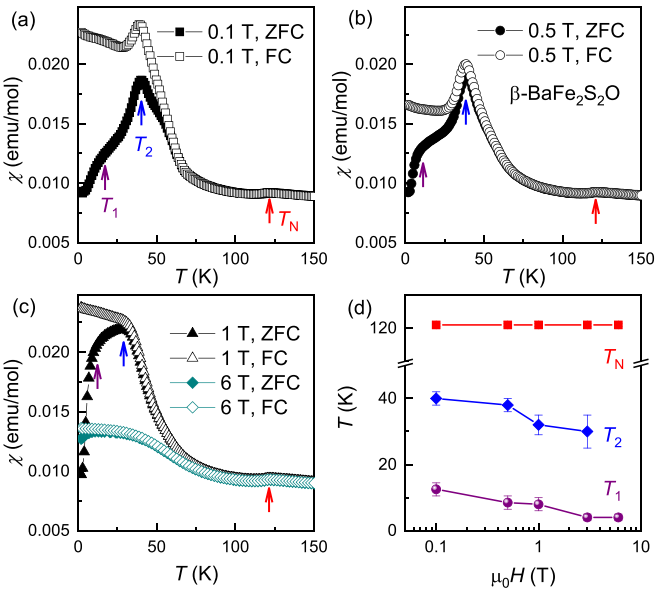

FIG. 4. [(a)–(c)] Temperature dependence of magnetic susceptibility of β-$BaFe_2S_2O$ measured at different magnetic fields in field-cooling (FC) and zero-field-cooling (ZFC) protocols. (d) Field dependence of the characteristic temperatures, T_1, T_2, and T_N, all of which are marked in (a)–(c).

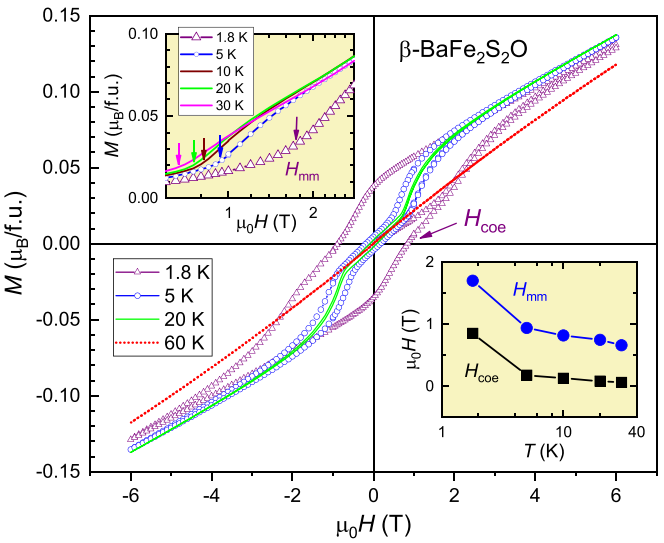

FIG. 5. Magnetic field dependence of magnetization at fixed temperatures for β-$BaFe_2S_2O$. The upper-left inset is a close-up of the initial $M(H)$ curves, in which the metamagnetic-like transitions at H_{mm} are marked by arrows. The lower-right inset plots H_{mm} and the coercive force H_{cov} as functions of temperature. Both inset plots employ a logarithmic scale for the horizontal axes.

correlations above T_N. As shown in the inset of Fig. 3, small deviations from the Curie-Weiss fit are clearly seen below 200 K, consistent with short-range AFM correlations.

The magnetic transition can be identified by the small peak at $T_N = 121$ K. Note that the T_N value is 15 K higher than that of β-$BaFe_2Se_2O$ [15]. A similar case can be seen in the other systems (see Table II). These observations suggest that the overall magnetic exchange interactions are enhanced with the replacement of Se by S. One notes that the T_N value is still much lower than the paramagnetic Weiss temperature θ_W, which implies existence of magnetic frustrations as suggested earlier [10].

There are additional magnetic anomalies below T_N. The FC and ZFC curves bifurcate at low temperatures. To clarify this phenomenon, we carried out the magnetic measurements with different applied fields. As shown in Fig. 4, one sees that the bifurcation exists up to 6 T. At lower fields (say, $\mu_0 H < 1$ T), a successive magnetic transition at $T_2 \approx 40$ K can be identified. Both χ_{ZFC} and χ_{FC} drop at T_2, suggesting an AFM-like transition (rather than a spin-glass transition). The transition temperature appears to decrease with increasing field. However, the transition itself changes from AFM-like to ferromagnetic (FM)-like. Furthermore, the temperature T_1, defined by the drop in χ_{ZFC}, also decreases with increasing field. By contrast, there is no detectable changes in T_N [see Fig. 4(d)].

Figure 5 shows the isothermal magnetization of β-$BaFe_2S_2O$ at some fixed temperatures below T_N. First of all, the magnetization is essentially linear with field at temperatures above T_2. Secondly, the $M(H)$ curve appears to be nonlinear with magnetic hysteresis below T_2. A metamagnetic-like transition can be detected, yet the magnetization does not saturate at the highest field applied. This kind of transition is not frequently seen, which basically rules out the possibility that the magnetic anomaly arises from extrinsic impurities. The metamagnetic-like behavior accounts for the above phenomenon showing AFM-to-FM-like crossover with increasing field. The metamagnetic transition field, $\mu_0 H_{mm}$, increases with decreasing temperature. Furthermore, the coercive force, $\mu_0 H_{coe}$, a characteristic parameter of a ferromagnet, shows a similar temperature dependence (see the lower inset of Fig. 5). Note that the remanent magnetization is only 0.037 μ_B/fu, suggesting a slight spin canting that generates the weak ferromagnetism. A similar magnetic hysteresis was observed in β-$BaFe_2Se_2O$ [15] and $Sr_2F_2Fe_2S_2O$ [17], although the remanent magnetization was even smaller there. The possible origin of the weak ferromagnetism will be discussed in the following sections.

The long-range magnetic ordering at T_N is confirmed by the specific-heat measurement. As shown in Fig. 6, a clear λ-shape peak appears at 120 K. Contrastingly, no discernible anomaly at around T_2 is present. The result indicates that the successive transition is associated with the change of spin orientations, rather than the change in spin ordering.

To extract the magnetic contribution, we employed a data fitting (the data from 76 to 152 K were not included) with combined Einstein and Debye models [34]. With the fitted data (red line in Fig. 6) representing the phonon contribution (C_{ph}), the magnetic contribution can be obtained with a simple subtraction, $C_m = C_{tot} - C_{ph}$. Then, the magnetic entropy associated with the magnetic ordering can be calculated using the integral $S_m = \int_0^T (C_m/T)dT$. One obtains an S_m value of 3.8 J K^{-1} mol^{-1} fu^{-1} above T_N, which is much smaller than the theoretical one, $S_m = 2R\ln(2S+1) = 26.8$ J K^{-1} mol^{-1} fu^{-1} (note that there are two Fe atoms in the

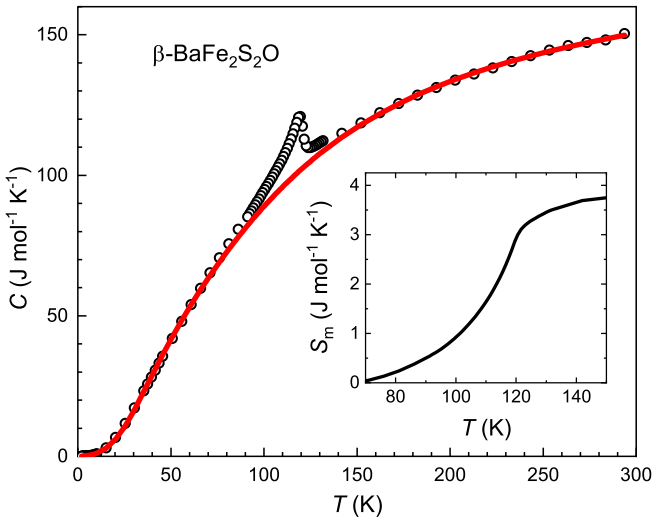

FIG. 6. Temperature dependence of specific heat for β-$BaFe_2S_2O$. The solid red line is the fitted data with combined Einstein and Debye models. The inset shows the released magnetic entropy associated with the long-range magnetic ordering.

formula unit of β-$BaFe_2S_2O$) for the high-spin ($S = 2$) Fe^{2+} moments. Similar results were reported in other related systems [12,13,15], which suggest existence of two-dimensional short-range spin correlations and/or a reduction of Fe^{2+} spins due to the d-p hybridizations.

Note that the T_N value of β-$BaFe_2S_2O$ is the highest among all the known oxychalcogenides with Fe_2OCh_2 layers (see Table II). Meanwhile, the interatomic distances of Fe-O and Fe-S in β-$BaFe_2S_2O$ are smallest among the oxychalcogenides. Thus it is possible to correlate T_N with the interatomic distances. Figures 7(a) and 7(b) plot T_N as functions of the interatomic distances of Fe-O and Fe-Ch, respectively, for the oxychalcogenides with Fe_2OCh_2 layers. One sees that T_N tends to increase with decreasing the bondlengths of Fe-O and Fe-Ch. The correlation between T_N and Fe-Se distance, yet not for the Fe-O bondlength, was earlier reported in the series of $R_2O_3Fe_2Se_2$ (R = Ce, Pr, Nd, and Sm) [13].

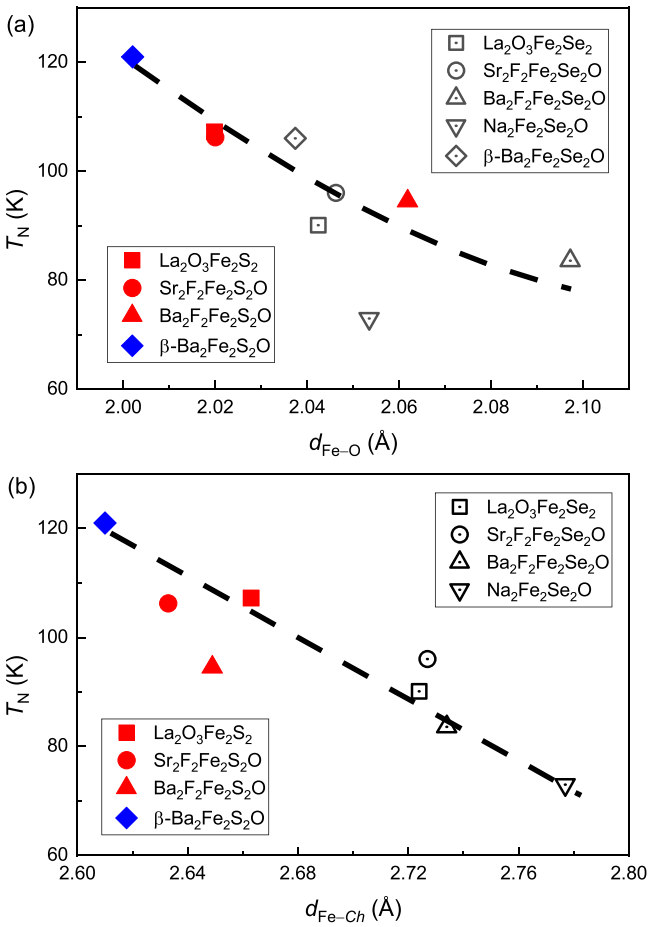

FIG. 7. Correlations between the Néel temperature, T_N, and the interatomic distances of Fe-O (a) and Fe-Ch (b) in the oxychalcogenides with Fe_2OCh_2 (Ch = Se, S) layers. The dashed lines are guides to the eye. The data of β-$BaFe_2S_2O$ are displayed with blue solid diamonds.

C. First-principles calculations

To understand the physical properties of β-$BaFe_2S_2O$ above, we carried out the DFT-based first-principles

TABLE III. Magnetic energy E_m (meV/fu) and magnetic moment μ_{Fe} (μ_B) of different magnetic structures of β-$BaFe_2S_2O$ with different values of U in the GGA+U calculations. NM, FM, S-AFM, C-AFM, and 2**k**-AFM respectively denote nonmagnetic, ferromagnetic, striped antiferromagnetic, Néel-type AFM, and checkerboard-like AFM. Owing to the negligibly small interlayer magnetic coupling, for simplicity and for comparison, the interplane orders are all ferromagnetic. The last three rows list the in-plane spin-exchange parameters, J_1, J_2, and J_2', within Ising model (see the text for details).

	0		1		2		3		4	
U (eV)	E_m	μ_{Fe}	E_m	μ_{Fe}	E_m	μ_{Fe}	E_m	μ_{Fe}	E_m	μ_{Fe}
NM	0	0	0	0	0	0	0	0	0	0
FM	−0.280	3.320	0.351	3.451	1.829	3.462	0.047	3.532	−0.130	3.575
S−AFM	−3.287	3.206	−64.338	3.328	−147.109	3.408	−145.545	3.473	−124.45	3.527
C−AFM	107.913	3.159	−15.013	3.315	−131.048	3.405	−145.306	3.473	−133.486	3.529
2**k**−AFM	−131.653	3.233	−131.361	3.335	−182.100	3.413	−166.912	3.476	−138.413	3.530
J_1 (meV)	−3.38		0.48		4.15		4.54		4.17	
J_2 (meV)	−8.02		−4.19		−2.19		−1.34		−0.87	
J_2' (meV)	11.59		7.75		7.34		5.89		4.48	

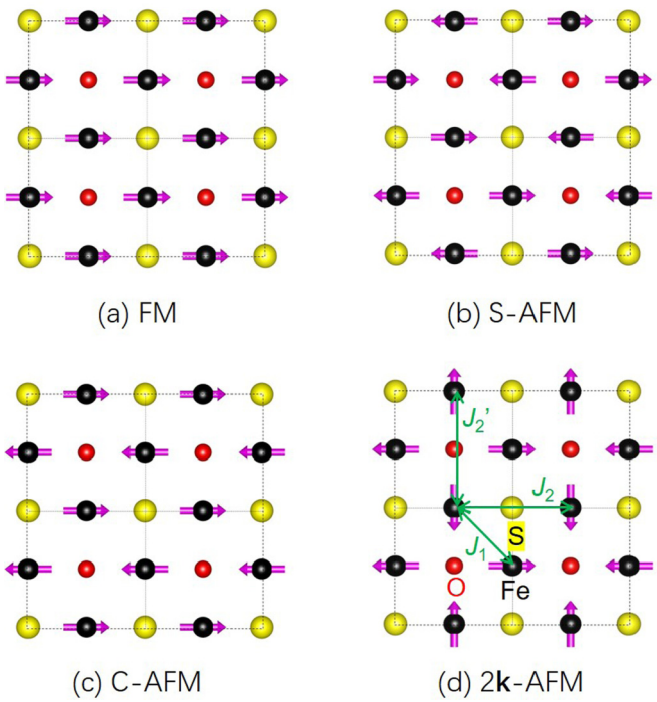

FIG. 8. Possible in-plane magnetic structures in β-$BaFe_2S_2O$ for the DFT-based calculations. FM (a), S-AFM (b), C-AFM (c), and 2**k**-AFM (d) represent ferromagnetic, striped AFM, Néel-type AFM, and the noncollinear AFM, respectively. The Fe^{2+} spins tend to align along the Fe-O bond direction due to spin-orbit coupling effect. Three intralayer magnetic exchange parameters, the nearest-neighbor J_1 and the next-nearest-neighbor J_2 and J_2', are marked in (d).

calculations. First we focus on the possible magnetic ground states, from which the dominant magnetic interactions can be evaluated. It is found that the magnetic energy hardly changes for a certain in-plane magnetic order yet with different spin arrangements along the c axis. This indicates that the intralayer magnetic interactions are predominant, consistent with the previous conclusion [17]. Thus, we considered four basic in-plane magnetic structures, as depicted in Fig. 8. The spin arrangement along the c axis was all assumed to be FM for simplicity. Furthermore, the spins are all along the Fe-O bond direction because of the spin-orbit-coupling induced magnetocrystalline anisotropy [15]. Such spin locking has been confirmed by lots of independent experiments for the related materials with common Fe_2OCh_2 layers [10,15,17,18,21,22].

Table III lists the magnetic energy (the energy of the nonmagnetic state is set to zero) and the corresponding Fe moment for different magnetic structures of β-$BaFe_2S_2O$ with varied U in the GGA+U calculations. For U values from 0 to 4 eV, the 2**k**-AFM configuration always gives the lowest energy, indicating the robustness of the 2**k**-AFM ground state. Meanwhile, the Fe moment remains to be 3.2–3.5 μ_B, close to the high-spin value of $\mu_{Fe} = gS = 4.0\,\mu_B$ (g is the Landé factor) and, independent of magnetic structures and U values. This calculation result is also consistent with those obtained by neutron scattering in other related systems [15,17,19,21]. The small reduction of the Fe moment is likely attributed to the p-d hybridizations. As stated above, the spin alignment along c axis does not change the magnetic energy within the calculation accuracy. Nevertheless, we argue that the real spin structure is most probably the in-plane 2**k**-AFM order and inter-plane AFM spin alignment along the c axis because of the Mott insulating state (see below). Namely, the magnetic propagation vectors are $\mathbf{k_1} = (1/2, 0, 1/2)$ and $\mathbf{k_2} = (0, 1/2, 1/2)$, which are identical to those of β-$BaFe_2Se_2O$ [15].

In view of the crystal structure of the Fe_2OS_2 layers, the effective magnetic interactions between Fe^{2+} spins can be modelled by (i) the nearest-neighbor coupling J_1, (ii) the next-nearest-neighbor J_2 with ~90° Fe-S-Fe superexchange, and (iii) the next-nearest-neighbor J_2' with 180° Fe-O-Fe superexchange, in accordance with the previous convention [6,18,22]. J_1 is contributed from direct Fe-Fe exchange, ~65° Fe-S-Fe superexchange, and 90° Fe-O-Fe superexchange. The magnetic energies of the four magnetic structures shown in Fig. 8 can be expressed in terms of the J_1-J_2-J_2' model using Heisenberg Hamiltonian, $H = \sum_{\langle i,j\rangle} J_{ij}\mathbf{S_i}\cdot\mathbf{S_j}$,

$$E_{FM} - E_0 = (4J_1 + 2J_2 + 2J_2')S^2, \tag{1a}$$

$$E_S - E_0 = (-2J_2 - 2J_2')S^2, \tag{1b}$$

$$E_C - E_0 = (-4J_1 + 2J_2 + 2J_2')S^2, \tag{1c}$$

$$E_{2k} - E_0 = (2J_2 - 2J_2')S^2, \tag{1d}$$

where E_{FM}, E_S, E_C, and E_{2k} denote the magnetic energy of the four magnetic structures, respectively, and E_0 is an accessorial parameter, which equivalently describes the energy of hypothetical spin-disordered state within the J_1-J_2-J_2' model. With $S^2 = 4$ for purely localized high-spin Fe^{2+}, the three spin-exchange parameters, J_1, J_2, and J_2', can be derived, which are listed in Table III. The results show that the oxygen-mediated 180° superexchange interaction is always AFM, and the sulfur-mediated ~90° superexchange is FM. This is consistent with the Goodenough-Kanamori rule [37–39], the latter of which predicts AFM coupling for 180° Fe-O-Fe superexchange and FM coupling for 90° Fe-S-Fe superexchange. The calculation results are basically consistent with the previous literatures [10,17,18,22]. Note that the AFM and the FM couplings synergistically favor the 2**k**-AFM order, according to Eq. (1d). Since J_2 and J_2' increases with the decrease of the bond lengths of Fe-O and Fe-Ch, respectively, the structural correlations on T_N shown in Fig. 7 can thus be naturally understood.

Figure 9 shows the energy dependence of density of states (DOS) projected on each atom for β-$BaFe_2S_2O$. One sees that the DOS near the Fermi energy E_F is dominated by Fe (3d electrons). By contrast, other elements contribute negligible DOS at around E_F. In the nonpolarized calculation [Fig. 9(a)], the overall bandwidth is 2.7 eV, which is significantly lower than that of LaFeAsO (4.2 eV) [40]. Such band narrowing was argued to be responsible for the Mott localization in $La_2O_3Fe_2Ch_2$ [6,17]. Without the correction of on-site Coulomb repulsion (i.e., $U = 0$ eV), nonetheless, the calculations fails to show an insulating state (with nonzero DOS at E_F), even for the 2**k**-AFM state [Figs. 9(a) and 9(b)]. This suggests that the GGA underestimates the electron correlations in the present case. We find that, with switching on an additional Coulomb repulsion with $U = 1$ eV [41],

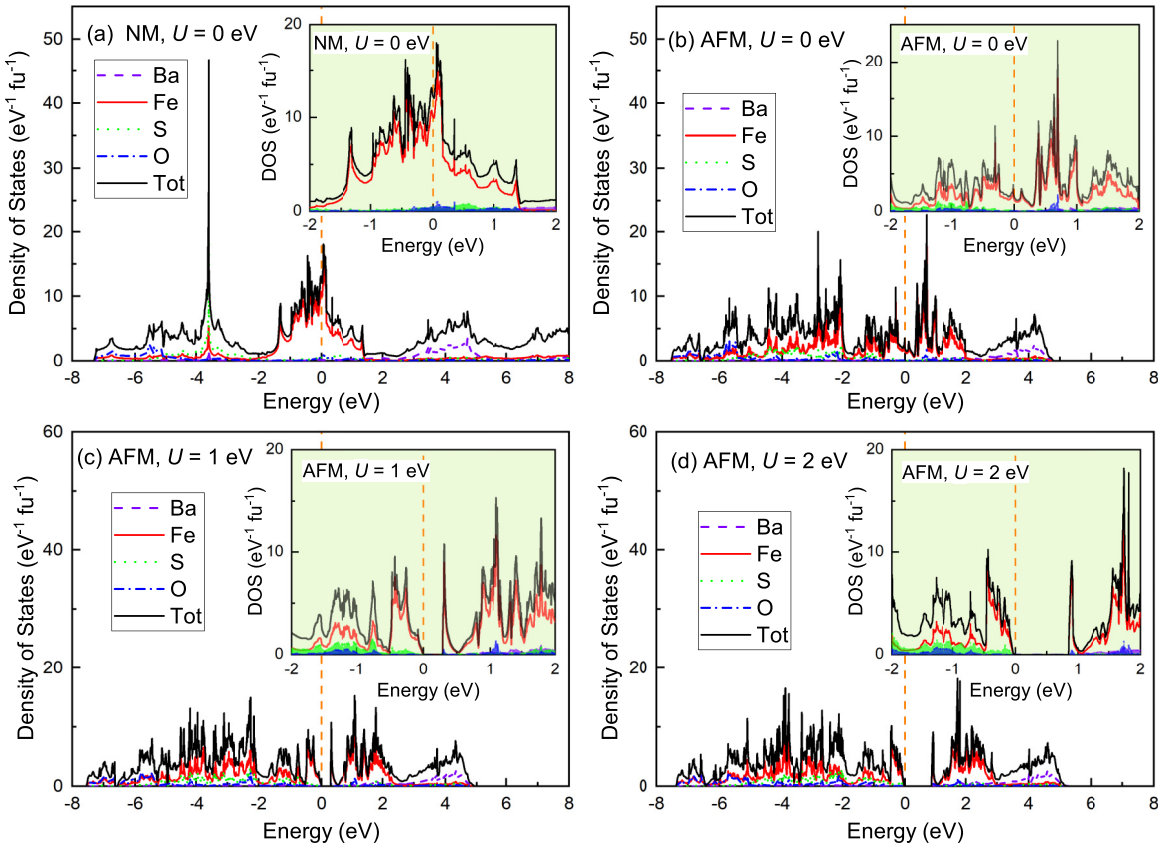

FIG. 9. Energy-dispersive density of states (DOS) projected on each atom for β-$BaFe_2S_2O$. (a) shows the nonpolarized calculation result without plus U. (b)–(d) are based on 2**k**-AFM order with $U = 0$, 1, and 2 eV, respectively. The insets display the close-ups showing the DOS around the Fermi level, $E_F = 0$.

a band gap of ∼0.3 eV opens at E_F. This calculated value is very close to the lower limit of the band gap from the resistivity measurement. Furthermore, the band gap increases with increasing U, which suggests that the insulating behavior is related to electron correlation effect. The Mott nature of the insulating state was also concluded from those complex calculations based on dynamical mean field theory [7,8]. One also notes that, experimentally, the system remains to be insulating even above the AFM Néel temperature. This verifies that the insulating behavior does not depend on the AFM order, which further corroborates the Mott insulating scenario in the title material.

D. Discussion

The title material β-$BaFe_2S_2O$ synthesized and investigated in this work is isostructural to β-$BaFe_2Se_2O$. While the replacement of Se with S leads to significant lattice contractions, the basic physical properties, such as insulating behavior and 2**k**-AFM spin order, remain. This is because the Fe-3d bandwidth is still lower than the on-site Coulomb interaction, which gives rise to Mott localization. Note that the special crystalline field with mixed-anion coordination octahedron of FeO_2Ch_4 helps the orbital-selective Mott localization [7] and the 2**k**-AFM spin order [15]. In order to drive the system to a metallic and/or superconducting state with suppressing the AFM order, we suggest that carrier doping should be more efficient than an isovalent element substitution.

The noncollinear magnetic order with orthogonal AFM chains is not only seen in the oxychalcogenides with Fe_2OCh_2 layers, but also appears in cobalt oxychalcogenides with Co_2OSe_2 layers [42] and even in superconducting iron pnictides of Ni-doped $CaKFe_4As_4$ [43]. The main difference in the latter cases is that the interchain coupling is also AFM, which leads to looplike spin-vortex structure [14,44] and hedgehog-like spin order [43,45]. The magnetic propagation vector is $\mathbf{k} = (1/2,1/2,l)$, which is different from the 2**k**-AFM spin order in the iron oxychalcogenides. Note that the magnetic structure of the isostructural manganese oxychalcogenides is a simple G-type AFM order with $\mathbf{k} = (0,0,0)$ [14,46], which implies the important role of spin-orbit coupling. Thus, stabilization of the unusual 2**k**-AFM spin order is attributed to the next-nearest-neighbor superexchange interactions, J_2 and J_2', in combination with the magnetocrystalline anisotropy.

Finally, we discuss on the possible origin of the weak ferromagnetism at low temperatures in β-$BaFe_2S_2O$ and other related materials. The basic fact is that the remanent magnetization is two or three orders of magnitude smaller than the full FM magnetization of Fe^{2+} spins. The result is reminiscent of the Dzyaloshinskii-Moriya (DM) superexchange interactions [47,48], which often give rise to a slight spin canting. In the case of Fe_2OCh_2 layers, the noncollinear spin order as well as some noncentrosymmetric superexchange

interactions guarantees a nonzero DM interaction. Therefore the successive magnetic transition and metamagnetic-like transition in β-$BaFe_2S_2O$ can be explained in terms of such DM interactions.

IV. CONCLUSION

In summary, we have successfully synthesized a new polymorph of iron-based oxychalcogenide, β-$BaFe_2S_2O$, at high pressures. This tetragonal polymorph belongs to the class of iron oxychalcogenides containing the characteristic Fe_2OCh_2 layers. Compared with the analogous oxyselenide of β-$BaFe_2Se_2O$, the title oxysulfide has significantly smaller lattice constants with reduced Fe-O and Fe-S bond lengths. As a result, the AFM Néel temperature is increased up to 121 K, which is so far record high among the class of iron oxychalcogenides. Nevertheless, the charge-transport activation energy remains unchanged. We have also identified a successive magnetic transition at ~40 K, which is likely to be associated with spin canting due to DM superexchange interactions. According to our first-principles calculations, a noncollinear AFM state with the multiple propagation vectors of $\mathbf{k_1} = (1/2,0,1/2)$ and $\mathbf{k_2} = (0,1/2,1/2)$ is mostly stabilized. The stabilization of this unusual spin order is associated with the magnetocrystalline anisotropy of Fe^{2+} spins as well as the oxygen-mediated antiferromagnetic superexchange and the sulfur-mediated ferromagnetic superexchange interactions. The insulating state is driven by on-site electron-electron Coulomb repulsion, demonstrating that the title material is a $3d^6$ Mott insulator. To further understand the relation between Mottness and superconductivity, one expects to be able to tune the system towards superconductivity by chemical doping and/or by applying pressures in future studies.

ACKNOWLEDGMENTS

This work was supported by the National Natural Science Foundation of China (12005003), the National Key R&D Program of China (2017YFA0303002), and the Key R&D Program of Zhejiang Province, China (2021C01002).

[1] J. G. Bednorz and K. A. Müller, Possible high T_c superconductivity in the Ba-La-Cu-O system, Z. Phys. B: Condens. Matter **64**, 189 (1986).

[2] P. A. Lee, N. Nagaosa, and X.-G. Wen, Doping a Mott insulator: Physics of high-temperature superconductivity, Rev. Mod. Phys. **78**, 17 (2006).

[3] Y. Kamihara, T. Watanabe, M. Hirano, and H. Hosono, Iron-based layered superconductor $La[O_{1-x}F_x]FeAs$ ($x = 0.05 - 0.12$) with $T_c = 26$ K, J. Am. Chem. Soc. **130**, 3296 (2008).

[4] D. C. Johnston, The puzzle of high temperature superconductivity in layered iron pnictides and chalcogenides, Adv. Phys. **59**, 803 (2010).

[5] Q. Si, R. Yu, and E. Abrahams, High-temperature superconductivity in iron pnictides and chalcogenides, Nat. Rev. Mater. **1**, 16017 (2016).

[6] J. X. Zhu, R. Yu, H. Wang, L. L. Zhao, M. D. Jones, J. Dai, E. Abrahams, E. Morosan, M. Fang, and Q. Si, Band Narrowing and Mott Localization in Iron Oxychalcogenides $La_2O_2Fe_2O(Se, S)_2$, Phys. Rev. Lett. **104**, 216405 (2010).

[7] G. Giovannetti, L. de' Medici, M. Aichhorn, and M. Capone, $La_2O_3Fe_2Se_2$: A Mott insulator on the brink of orbital-selective metallization, Phys. Rev. B **91**, 085124 (2015).

[8] B. Freelon, Y. H. Liu, J.-L. Chen, L. Craco, M. S. Laad, S. Leoni, J. Chen, L. Tao, H. Wang, R. Flauca, Z. Yamani, M. Fang, C. Chang, J.-H. Guo, and Z. Hussain, Mott-Kondo insulator behavior in the iron oxychalcogenides, Phys. Rev. B **92**, 155139 (2015).

[9] J. M. Mayer, L. F. Schneemeyer, T. Siegrist, J. V. Waszczak, and B. Van Dover, New layered iron-lanthanum-oxide-sulfide and -selenide phases: $Fe_2La_2O_3E_2$ (E = S, Se), Angew. Chem. Int. Ed. Engl. **31**, 1645 (1992).

[10] H. Kabbour, E. Janod, B. Corraze, M. Danot, C. Lee, M.-H. Whangbo, and L. Cario, Structure and magnetic properties of oxychalcogenides $A_2F_2Fe_2OQ_2$(A = Sr, Ba; Q = S, Se) with Fe_2O square planar layers representing an antiferromagnetic checkerboard spin lattice, J. Am. Chem. Soc. **130**, 8261 (2008).

[11] Y. Fuwa, M. Wakeshima, and Y. Hinatsu, Crystal structure, magnetic properties, and Mossbauer spectroscopy of new layered iron oxyselenide $Nd_2Fe_2O_3Se_2$, J. Phys.: Condens. Matter **22**, 346003 (2010).

[12] J. B. He, D. M. Wang, H. L. Shi, H. X. Yang, J. Q. Li, and G. F. Chen, Synthesis, structure, and magnetic properties of the layered iron oxychalcogenide $Na_2Fe_2Se_2O$, Phys. Rev. B **84**, 205212 (2011).

[13] N. Ni, S. Jia, Q. Huang, E. Climent-Pascual, and R. J. Cava, Structural, transport, thermodynamic, and neutron diffraction studies of layered $R_2O_3Fe_2Se_2$ (R = Ce, Pr, Nd, and Sm), Phys. Rev. B **83**, 224403 (2011).

[14] D. G. Free, N. D. Withers, P. J. Hickey, and J. S. O. Evans, Synthesis, structure and properties of several new oxychalcogenide materials with the general formula $A_2O_2M_2OSe_2$(A = La - Sm, M = Fe, Mn), Chem. Mater. **23**, 1625 (2011).

[15] F. Takeiri, Y. Matsumoto, T. Yamamoto, N. Hayashi, Z. Li, T. Tohyama, C. Tassel, C. Ritter, Y. Narumi, M. Hagiwara, and H. Kageyama, High-pressure synthesis of the layered iron oxyselenide $BaFe_2Se_2O$ with strong magnetic anisotropy, Phys. Rev. B **94**, 184426 (2016).

[16] C. Stock and E. E. McCabe, The magnetic and electronic properties of oxyselenides—influence of transition metal ions and lanthanides, J. Phys.: Condens. Matter **28**, 453001 (2016).

[17] L. L. Zhao, S. Wu, J. K. Wang, J. P. Hodges, C. Broholm, and E. Morosan, Quasi-two-dimensional noncollinear magnetism in the Mott insulator $Sr_2F_2Fe_2OS_2$, Phys. Rev. B **87**, 020406(R) (2013).

[18] E. E. McCabe, C. Stock, E. E. Rodriguez, A. S. Wills, J. W. Taylor, and J. S. O. Evans, Weak spin interactions in Mott insulating $La_2O_2Fe_2OSe_2$, Phys. Rev. B **89**, 100402(R) (2014).

[19] M. Günther, S. Kamusella, R. Sarkar, T. Goltz, H. Luetkens, G. Pascua, S.-H. Do, K.-Y. Choi, H. D. Zhou, C. G. F. Blum, S. Wurmehl, B. Büchner, and H.-H. Klauss, Magnetic order and spin dynamics in $La_2O_2Fe_2OSe_2$ probed by ^{57}Fe Mössbauer,

^{139}La NMR, and muon-spin relaxation spectroscopy, Phys. Rev. B **90**, 184408 (2014).

[20] E. E. McCabe, A. S. Wills, L. Chapon, P. Manuel, and J. S. O. Evans, Structural and magnetic characterization of iron oxyselenides $Ce_2O_2Fe_2OSe_2$ and $Nd_2O_2Fe_2OSe_2$, Phys. Rev. B **90**, 165111 (2014).

[21] R. K. Oogarah, E. Suard, and E. E. McCabe, Magnetic order and phase transition in the iron oxysulfide $La_2O_2Fe_2OS_2$, J. Magn. Magn. Mater. **446**, 101 (2018).

[22] B. Freelon, Z. Yamani, I. Swainson, R. Flacau, B. Karki, Y. H. Liu, L. Craco, M. S. Laad, M. Wang, J. Chen, R. J. Birgeneau, and M. Fang, Magnetic and structural properties of the iron oxychalcogenides $La_2O_2Fe_2OM_2(M = S, Se)$, Phys. Rev. B **99**, 024109 (2019).

[23] F. Han, X. Wan, B. Shen, and H.-H. Wen, $BaFe_2Se_2O$ as an iron-based Mott insulator with antiferromagnetic order, Phys. Rev. B **86**, 014411 (2012).

[24] H. Lei, H. Ryu, V. Ivanovski, J. B. Warren, A. I. Frenkel, B. Cekic, W.-G. Yin, and C. Petrovic, Structure and physical properties of the layered iron oxychalcogenide $BaFe_2Se_2O$, Phys. Rev. B **86**, 195133 (2012).

[25] Z. V. Popović, M. Šćepanović, N. Lazarević, M. M. Radonjić, D. Tanasković, H. Lei, and C. Petrovic, Phonon and magnetic dimer excitations in Fe-based $S = 2$ spin-ladder compound $BaFe_2Se_2O$, Phys. Rev. B **89**, 014301 (2014).

[26] M. Valldor, P. Adler, Y. Prots, U. Burkhardt, and L. H. Tjeng, $S = 2$ spin ladders in the sulfide oxide $BaFe_2S_2O$, Eur. J. Inorg. Chem. **2014**, 6150 (2014).

[27] M. H. Fang, H. M. Pham, B. Qian, T. J. Liu, E. K. Vehstedt, Y. Liu, L. Spinu, and Z. Q. Mao, Superconductivity close to magnetic instability in $Fe(Se_{1-x}Te_x)_{0.82}$, Phys. Rev. B **78**, 224503 (2008).

[28] C. Wang, S. Jiang, Q. Tao, Z. Ren, Y. Li, L. Li, C. Feng, J. Dai, G. Cao, and Z. an Xu, Superconductivity in $LaFeAs_{1-x}P_xO$: Effect of chemical pressures and bond covalency, Europhys. Lett. **86**, 47002 (2009).

[29] X. Lai, H. Zhang, Y. Wang, X. Wang, X. Zhang, J. Lin, and F. Huang, Observation of superconductivity in tetragonal FeS, J. Am. Chem. Soc. **137**, 10148 (2015).

[30] F. Izumi and K. Momma, Three-dimensional visualization in powder diffraction, Solid State Phenom **130**, 15 (2007).

[31] G. Kresse and J. Furthmüller, Efficient iterative schemes for ab initio total-energy calculations using a plane-wave basis set, Phys. Rev. B **54**, 11169 (1996).

[32] J. P. Perdew, K. Burke, and M. Ernzerhof, Generalized Gradient Approximation Made Simple, Phys. Rev. Lett. **77**, 3865 (1996).

[33] S. L. Dudarev, G. A. Botton, S. Y. Savrasov, C. J. Humphreys, and A. P. Sutton, Electron-energy-loss spectra and the structural stability of nickel oxide: An LSDA+U study, Phys. Rev. B **57**, 1505 (1998).

[34] A. Ablimit, Y.-L. Sun, H. Jiang, S.-Q. Wu, Y.-B. Liu, and G.-H. Cao, Weak metal-metal transition in the vanadium oxytelluride $Rb_{1-\delta}V_2Te_2O$, Phys. Rev. B **97**, 214517 (2018).

[35] N. E. Brese and M. O'Keeffe, Bond-valence parameters for solids, Acta Crystallogr. Sect. B **47**, 192 (1991).

[36] J. Gamon, A. J. Perez, L. A. H. Jones, M. Zanella, L. M. Daniels, R. E. Morris, C. C. Tang, T. D. Veal, L. J. Hardwick, M. S. Dyer, J. B. Claridge, and M. J. Rosseinsky, $Na_2Fe_2OS_2$, a new earth abundant oxysulphide cathode material for Na-ion batteries, J. Mater. Chem. A **8**, 20553 (2020).

[37] J. B. Goodenough, Theory of the role of covalence in the perovskite-type manganites [La,M(II)]MnO_3, Phys. Rev. **100**, 564 (1955).

[38] J. B. Goodenough, An interpretation of the magnetic properties of the perovskite-type mixed crystals $La_{1-x}Sr_xCoO_{3-\lambda}$, J. Phys. Chem. Solids **6**, 287 (1958).

[39] J. Kanamori, Theory of the magnetic properties of ferrous and cobaltous oxides, I, Prog. Theor. Phys. **17**, 177 (1957).

[40] D. J. Singh and M.-H. Du, Density Functional Study of $LaFeAsO_{1-x}F_x$: A Low Carrier Density Superconductor Near Itinerant Magnetism, Phys. Rev. Lett. **100**, 237003 (2008).

[41] The U value basically represents the correction of the on-site Coulomb repulsion, rather than the Hubbard U_H itself.

[42] C. Wang, M.-Q. Tan, C.-M. Feng, Z.-F. Ma, S. Jiang, Z.-A. Xu, G.-H. Cao, K. Matsubayashi, and Y. Uwatoko, $La_2Co_2Se_2O_3$: A quasi-two-dimensional mott insulator with unusual cobalt spin state and possible orbital ordering, J. Am. Chem. Soc. **132**, 7069 (2010).

[43] A. Kreyssig, J. M. Wilde, A. E. Böhmer, W. Tian, W. R. Meier, B. Li, B. G. Ueland, M. Xu, S. L. Bud'ko, P. C. Canfield, R. J. McQueeney, and A. I. Goldman, Antiferromagnetic order in $CaK(Fe_{1-x}Ni_x)_4As_4$ and its interplay with superconductivity, Phys. Rev. B **97**, 224521 (2018).

[44] Y. Fuwa, T. Endo, M. Wakeshima, Y. Hinatsu, and K. Ohoyama, Orthogonal spin arrangement in quasi-two-dimensional $La_2Co_2O_3Se_2$, J. Am. Chem. Soc. **132**, 18020 (2010).

[45] W. R. Meier, Q.-P. Ding, A. Kreyssig, S. L. Bud'ko, A. Sapkota, K. Kothapalli, V. Borisov, R. Valentí, C. D. Batista, P. P. Orth, R. M. Fernandes, A. I. Goldman, Y. Furukawa, A. E. Böhmer, and P. C. Canfield, Hedgehog spin-vortex crystal stabilized in a hole-doped iron-based superconductor, npj Quantum Mater. **3**, 5 (2018).

[46] N. Ni, E. Climent-Pascual, S. Jia, Q. Huang, and R. J. Cava, Physical properties and magnetic structure of the layered oxyselenide $La_2O_3Mn_2Se_2$, Phys. Rev. B **82**, 214419 (2010).

[47] I. Dzyaloshinsky, A thermodynamic theory of weak ferromagnetism of antiferromagnetics, J. Phys. Chem. Solids **4**, 241 (1958).

[48] T. Moriya, Anisotropic superexchange interaction and weak ferromagnetism, Phys. Rev. **120**, 91 (1960).